

## Research Article

# Highly Active and Durable NiMoMn Hydrogen Evolution Catalysts for Proton-Exchange Membrane Water Electrolysis

Chan Hee Lee , Kyeong-Rim Yeo , and Soo-Kil Kim

School of Integrative Engineering, Chung-Ang University, Seoul 06974, Republic of Korea

Correspondence should be addressed to Soo-Kil Kim; [sookilkim@cau.ac.kr](mailto:sookilkim@cau.ac.kr)

Received 18 January 2025; Accepted 4 April 2025

Academic Editor: Denis Osinkin

Copyright © 2025 Chan Hee Lee et al. International Journal of Energy Research published by John Wiley & Sons Ltd. This is an open access article under the terms of the Creative Commons Attribution License, which permits use, distribution and reproduction in any medium, provided the original work is properly cited.

Proton-exchange membrane water electrolysis (PEMWE) powered by renewable energy sources is an eco-friendly technology for the mass production of hydrogen. One of the major obstacles in the commercialization of PEMWE is the necessity of using precious metal catalysts under corrosive operating conditions, which can be partially mitigated by using nonprecious metal catalysts for the cathode, where the conditions are less harsh than those for the anode. However, the use of nonprecious transition metal catalysts limits both performance and durability. To overcome this limitation, a wide range of NiMoMn ternary alloy catalyst compositions were fabricated by electrodeposition, and their performances were evaluated. The best-performing Ni<sub>82.1</sub>Mo<sub>11.6</sub>Mn<sub>6.3</sub> alloy catalyst exhibited an outstanding hydrogen evolution performance with an overpotential of 16 mV at  $-10 \text{ mA cm}^{-2}$ , and with an increase of only 8 mV after 10,000 potential cycles for durability testing. The application of this material in a PEMWE single cell gave a favorable performance of  $1.936 \text{ A cm}^{-2}$  at  $2.0 \text{ V}_{\text{cell}}$ , and an excellent degradation rate of  $2.2 \text{ mV h}^{-1}$  in a durability test performed at  $1 \text{ A cm}^{-2}$ . This high performance and excellent durability of the Ni<sub>82.1</sub>Mo<sub>11.6</sub>Mn<sub>6.3</sub> catalyst was attributed to the modulation of its electronic structure, in addition to a large electrochemical surface area, and stable Mn oxide formation on the surface. These results indicate the potential of this catalyst for use in lowering the hydrogen production costs associated with PEMWE.

**Keywords:** electrocatalyst; electrodeposition; hydrogen evolution reaction; NiMoMn; proton-exchange membrane water electrolysis

## 1. Introduction

The intermittent nature of electricity generated by renewable energy sources is known to place a load on the grid upon the production of excess electricity. This problem can be solved using an energy storage system (ESS) to store excess power by converting it to another energy type. Hydrogen has gained attention as an ESS due to its high energy density, stable storage, and zero carbon emissions during conversion. In addition, the electrolysis of water using renewable energy has been considered a promising eco-friendly method for hydrogen production due to the fact that it does not emit any pollutants [1, 2]. In this context, proton-exchange membrane water electrolysis (PEMWE) can offset the disadvantages of alkaline water electrolysis (AWE) and achieve low

ohmic losses, low gas crossovers, a compact design, high-purity hydrogen production, and a fast load fluctuation response [3]. However, since the PEMWE requires an acidic operating environment, the catalyst is limited to precious metals such as Pt, which exhibits a near-optimal hydrogen adsorption energy ( $\Delta G_H^*$ ) [4] in addition to good corrosion resistance. Furthermore, it has been reported that linking PEMWE to renewable energy sources leads to a fluctuating operating potential, thereby necessitating a material that exhibits sufficient durability under such conditions [5]. In particular, catalysts for the oxygen evolution reaction (OER) are inevitably limited to precious metals because of their operating potentials exceeding  $>1.23 \text{ V}_{\text{RHE}}$ . Consequently, the high cost of precious metals is a major barrier to the commercialization of PEMWE systems.

However, in the case of the hydrogen evolution reaction (HER), a negative overpotential is applied with respect to  $0 V_{\text{RHE}}$ , thereby partially eliminating the necessity of using precious metals. Although there are some opportunities to use nonprecious HER catalysts in PEMWE, these materials remain vulnerable to high potentials and acidic environments, resulting in chemical and structural changes, such as delamination of the catalyst layer from the substrate, and changes in its composition due to dissolution, ultimately leading to a reduced catalytic activity [6]. To address these challenges, various strategies have been developed to enhance the activity and durability of nonprecious HER catalysts, including compound selection, alloying, and structural engineering. For example, the incorporation of additional compounds and alloys can optimize the  $(\Delta G_H^*)$  value on the catalyst surface by altering its electronic structure, thereby enhancing the intrinsic activity of the catalyst [4, 7]. Representative examples of these compounds include the phosphides, sulfides, and carbides of transition metals [8, 9]. Differences in electronegativity between phosphorus/sulfur and transition metals modify the catalyst's electronic structure, optimizing hydrogen adsorption, enhancing acidic HER activity, and improving durability at optimal contents [10]. Example compounds include NiP [11], CoP [12], MoP [13], and FeP [14]. In addition, Xie et al. [15] prepared an FeP/Ti catalyst by the deposition of a FeOOH film on Ti foil using electrodeposition followed by phosphorization. The as-prepared FeP/Ti catalyst demonstrated a good performance with overpotentials of 79 and 95 mV at  $-10 \text{ mA cm}^{-2}$  in 0.5 M  $\text{H}_2\text{SO}_4$  and 1 M KOH solutions, respectively. A stability test confirmed the durability of this catalyst over a period of 8–10 h. Among the sulfide-based nonprecious-metal catalysts,  $\text{MoS}_2$  is generally the most studied, exhibiting a high activity with an almost optimal  $(\Delta G_H^*)$  value of 0.08 eV for the edge sites [16, 17]. Subsequently, it was found that increasing the exposure of the edge sites through nanowall formation [18] led to an overpotential of 95 mV at  $-10 \text{ mA cm}^{-2}$  and a Tafel slope of  $78 \text{ mV dec}^{-1}$  in acidic solutions. In addition, Nguyen et al. [19] synthesized a nanoflower heterostructure composed of  $\text{MoS}_2$  and  $\text{WS}_2$ , attributing its remarkable HER performance to the unique interfacial properties between the two materials. Carbide-based nonprecious metal catalysts have also been reported to exhibit surface properties and performances comparable to those of Pt [8]. For example, Xiao et al. [20] prepared a bimetallic carbide nanostructure consisting of  $\text{Mo}_2\text{C}$  and WC catalysts, resulting in an overpotential of 184 mV at  $-10 \text{ mA cm}^{-2}$ , along with no significant change in activity after 3,000 cycles.

In terms of the alloy catalysts, Ni- and Cu-based bimetallic alloys have been widely studied owing to their relatively high intrinsic activities in the acidic HER, and their superior durability, which can be attributed to their more positive standard reduction potentials compared to those of other transition metals [21–25]. For example, Deng et al. [23] prepared a  $\text{CoNi@NC}$  catalyst via a bottom-up approach using ethylenediaminetetraacetate anions, and the prepared catalyst demonstrated an overpotential of 142 mV at  $-10 \text{ mA cm}^{-2}$  with a Tafel slope of  $104 \text{ mV dec}^{-1}$ . In another study,

Kim et al. [24] used the electrodeposition technique to fabricate a  $\text{Co}_{59}\text{Cu}_{41}$  catalyst, leading to an overpotential of 342 mV at  $-10 \text{ mA cm}^{-2}$  and a Tafel slope of  $103 \text{ mV dec}^{-1}$  in a 0.5 M  $\text{H}_2\text{SO}_4$  solution. They also prepared a  $\text{Cu}_{99.2}\text{Mo}_{0.8}$  catalyst [25] with a mass activity of  $233.4 \text{ mA mg}_{\text{Cu+Mo}}^{-1}$  and a Tafel slope of  $94 \text{ mV dec}^{-1}$  in an acidic solution. In addition to Ni and Cu, Mn-based catalysts have also been subjected to modification using single atoms, alloys, doping, and morphological changes, generating efficient catalysts for application in the HER [26]. For instance, Liu et al. [27] prepared MnCoP/Ti catalysts by electrodeposition and heat treatment, which exhibited an overpotential of 49 mV at  $-10 \text{ mA cm}^{-2}$  in a 0.5 M  $\text{H}_2\text{SO}_4$  solution. Furthermore, Guo et al. [28] prepared a NiMnS/Ti by electrodeposition on Ti paper. Compared to the corresponding NiS/Ti catalyst, the hollow structure of the NiMnS/Ti catalyst led to a 37 mV reduction in the overpotential.

Among the binary alloy catalysts with moderate durability, NiMo is known to possess an extremely high acidic HER activity [29–33]. For instance, McKone et al. [33] reported that a NiMo catalyst with a composition ratio of 6.4:3.6 exhibited an HER overpotential of 80 mV at  $-20 \text{ mA cm}^{-2}$ , along with a decay rate of  $2.8 \text{ mV h}^{-1}$  over 10 h. This study, therefore, aims to further enhance the activity and durability of NiMo by the addition of Mn as a third component. More specifically, a ternary alloy catalyst composed of Ni, Mo, and Mn is fabricated via electrodeposition, and subsequently, its applicability is verified on both the half-cell and PEMWE single-cell levels. Various combinations of these three components are investigated to determine the optimal composition for maximizing the HER performance. Physicochemical and electrochemical analyses are also performed to determine the factors responsible for enhanced HER activity and durability. Notably, the electrodeposition approach, which is considered to be one of the best methods for fabricating catalyst-coated porous transport electrodes [34, 35], is used throughout to deposit the NiMoMn catalysts on carbon paper, due to its ability to rapidly produce metal nanostructures under atmospheric conditions, with strong bonding between the catalyst and the porous transport layer.

## 2. Materials and Methods

**2.1. Catalyst Preparation.** The NiMoMn catalysts were prepared using a one-step electrodeposition method. All catalysts were electrodeposited in a homemade three-electrode Teflon cell at ambient pressure and room temperature. A saturated calomel electrode ([SCE], CHI 150) and a graphite rod were used as reference and counter electrodes, respectively. Carbon paper (Ballard, Avcarb MGL280) with an exposed area of  $1.43 \text{ cm}^2$  was used as the substrate for electrodeposition. The solution for electrodeposition was prepared by mixing  $\text{C}_6\text{H}_5\text{Na}_3\text{O}_7 \cdot 2\text{H}_2\text{O}$  (7555-4405, Daejung),  $\text{MnCl}_2 \cdot 4\text{H}_2\text{O}$  (19285S0301, Junsei),  $\text{Na}_2\text{MoO}_4 \cdot 2\text{H}_2\text{O}$  (7598-4405, Daejung), and  $\text{NiCl}_2 \cdot 6\text{H}_2\text{O}$  (141-01045, Waco) in deionized water ( $18.2 \text{ M}\Omega \text{ cm}$ ) with stirring for 20 min to prepare a solution with a total volume of 40 mL. Details regarding the quantities of all reagents employed for

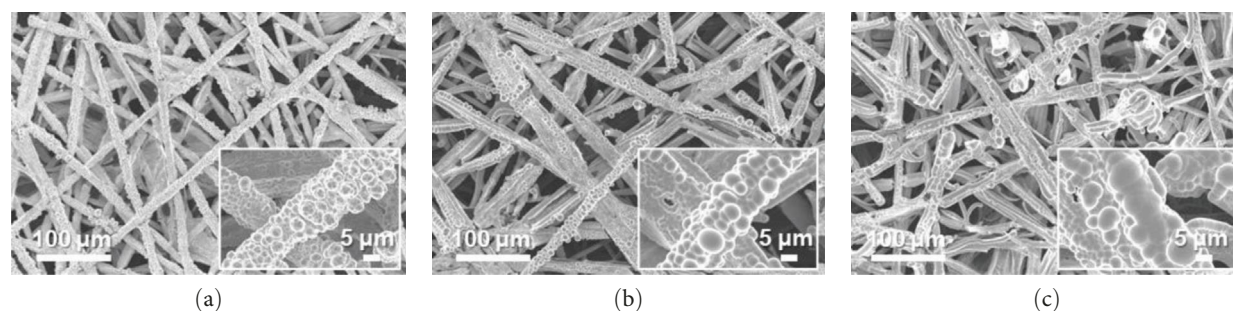


FIGURE 1: FE-SEM images of the (a)  $\text{Ni}_{100}$ , (b)  $\text{Ni}_{94.6}\text{Mo}_{5.4}$ , and (c)  $\text{Ni}_{82.1}\text{Mo}_{11.6}\text{Mn}_{6.3}$  species. The insets show the corresponding FE-SEM images at higher magnifications.

fabrication of the various NiMoMn catalysts are summarized in Table S1. The solution was then purged with  $\text{N}_2$  for 30 min to eliminate any dissolved oxygen. Subsequently, electrodeposition was performed by applying a constant potential of  $-2 \text{ V}_{\text{SCE}}$  for 10 min (CS350, Wuhan CorrTest Instrument Corp., Ltd.). The resulting catalysts deposited on the carbon paper were rinsed using deionized water for 20 s and dried under a flow of  $\text{N}_2$  gas. For the best performing sample, a heat treatment was conducted at  $200^\circ\text{C}$  for 2 h in a 4%  $\text{H}_2/\text{Ar}$  atmosphere to investigate its effects on the performance and durability of the catalyst.

**2.2. Material Characterization.** Field emission scanning electron microscopy ([FE-SEM], Zeiss Sigma) was performed to observe the morphologies of the catalysts. The bulk compositions of the catalysts were evaluated using energy dispersive X-ray spectroscopy (EDS, Noran System 7, Thermo Fisher). X-ray diffractometry ([XRD], NEW D8-Advance, Bruker-AXS) was conducted to collect information regarding the crystal structures of catalysts. XRD was performed between  $2\theta$  values of  $20\text{--}80^\circ$  at a scan rate of  $1^\circ \text{ min}^{-1}$ . The electronic structure, oxidation state, and composition of the catalyst surface were investigated using X-ray photoelectron spectroscopy ([XPS], K-alpha+, Thermo Fisher Scientific) with calibration based on the binding energy ( $284.6 \text{ eV}$ ) of the C 1s C–C peak.

**2.3. Electrochemical Characterization.** The HER performance was measured by cyclic voltammetry (CV) between  $-0.23$  and  $0.07 \text{ V}_{\text{RHE}}$  at a scan rate of  $1 \text{ mV s}^{-1}$ . HER polarization curves were obtained after iR-compensation using the ohmic resistance obtained by electrochemical impedance spectroscopy (EIS). The electrochemical double-layer capacitances were measured by linear sweep voltammetry (LSV) in the nonfaradaic potential region at scan rates ranging from 10 to  $100 \text{ mV s}^{-1}$  in a 1 M NaOH solution. An accelerated degradation test (ADT) was performed for the catalyst over 10,000 CV cycles between  $-0.2$  and  $0.05 \text{ V}_{\text{RHE}}$  at a scan rate of  $100 \text{ mV s}^{-1}$ . A constant current durability test was also carried out at  $-10 \text{ mA cm}^{-2}$  for 24 h. All electrochemical measurements were performed using a three-electrode system in an acidic solution ( $0.5 \text{ M H}_2\text{SO}_4$ ).

**2.4. PEMWE Performance Measurements.** To prepare a membrane electrode assembly (MEA) with an active area of  $1 \text{ cm}^2$ , the best-performing NiMoMn catalyst deposited on carbon paper was used as the cathode. The anode was fabricated by

spray coating commercial iridium oxide (043396, Alfa Aesar) on carbon paper with a loading of  $2.0 \text{ mg cm}^{-2}$ . The prepared electrodes were placed on both sides of a Nafion 212 membrane (DuPont,  $50.8 \mu\text{m}$  thickness) without hot-pressing. In our study, hot pressing was not used in MEA fabrication because electrodeposition provides strong catalyst adhesion, uniform distribution, and optimal performance without the need for thermal or mechanical stress, preserving membrane integrity and simplifying the manufacturing process. The resulting PEMWE was operated at  $90^\circ\text{C}$ , and a flow of preheated deionized water was introduced into the anode line at a rate of  $15 \text{ mL min}^{-1}$ . The PEMWE performance was measured by performing 30 min of activation at  $2.2 \text{ V}_{\text{cell}}$  followed by a backward scan from 2.2 to  $1.35 \text{ V}_{\text{cell}}$  at 0.05 V intervals, holding for 1 min at each interval. These steps were repeated three times prior to carrying out the performance evaluation. Additionally, a constant-current durability test was performed at  $1 \text{ A cm}^{-2}$  for 24 h. The catalyst loading amounts before and after the single-cell durability test were quantitatively analyzed using inductively coupled plasma mass spectrometry ([ICP-MS], 7900, Agilent). To assess the extent of metal leaching, the effluent discharged from the single cell over a 24-h period was collected and subjected to ICP-MS analysis.

### 3. Results and Discussion

**3.1. Catalyst Characterization.** FE-SEM and EDS analyses were performed on the deposited catalysts to observe the effects of the precursor ratio on the catalyst morphology and composition. Figure 1 shows SEM images of representative  $\text{Ni}_{100}$ ,  $\text{Ni}_{94.6}\text{Mo}_{5.4}$ , and  $\text{Ni}_{82.1}\text{Mo}_{11.6}\text{Mn}_{6.3}$  specimens. For the  $\text{Ni}_{100}$  catalyst, spherical particles with diameters of  $0.5\text{--}2 \mu\text{m}$  were observed to densely cover the carbon paper (Figure 1a). Upon the addition of a small amount of Mo, larger  $\text{Ni}_{94.6}\text{Mo}_{5.4}$  catalyst particles were evident on the carbon paper surface (Figure 1b), and upon the incorporation of Mn, the  $\text{Ni}_{82.1}\text{Mo}_{11.6}\text{Mn}_{6.3}$  catalyst produced smoother deposits on the support surface (Figure 1c), exhibiting almost no separated aggregates. These changes in the surface morphology in the presence of Mn are consistent with the observations of previous studies [36–38]. Notably, all three catalysts showed complete coverage of the carbon fibers and very uniform distribution over the entire carbon substrates (Figure S1).

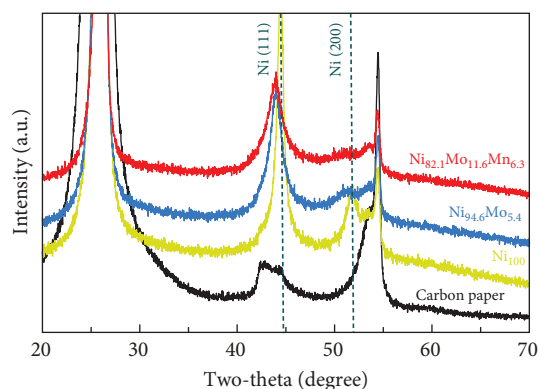


FIGURE 2: XRD patterns of the  $\text{Ni}_{100}$ ,  $\text{Ni}_{94.6}\text{Mo}_{5.4}$ , and  $\text{Ni}_{82.1}\text{Mo}_{11.6}\text{Mn}_{6.3}$  species.

Subsequently, the crystal structures of the three catalysts were examined using XRD, as presented in Figure 2. The carbon paper used as the substrate exhibited sharp peaks at  $42.46^\circ$ ,  $43.02^\circ$ ,  $44.67^\circ$ ,  $47.37^\circ$ , and  $54.8^\circ$  (JCPDS# 26-1080). For the  $\text{Ni}_{100}$  catalyst, Ni peaks corresponding to the face-centered cubic (111) and (200) planes were clearly observed at  $44.5^\circ$  and  $51.8^\circ$ , respectively (JCPDS# 04-0850). When comparing the Ni (111) peaks of the  $\text{Ni}_{100}$  and  $\text{Ni}_{94.6}\text{Mo}_{5.4}$  catalyst, it was found that the peak intensity decreased and the peak shifted to a lower angle with the addition of Mo, which was likely caused by lattice expansion due to the larger radius of Mo (0.145 nm) compared to that of Ni (0.135 nm), confirming a less developed alloy structure [29, 39–41]. Notably, no peaks corresponding to Mo were observed. In the case of  $\text{Ni}_{82.1}\text{Mo}_{11.6}\text{Mn}_{6.3}$ , when comparing the Ni (111) and Ni (200) peaks, it was found that the peak intensity was further reduced while the peak position was maintained, thereby indicating the presence of a ternary alloy with a reduced crystallinity.

The surface elemental compositions, electronic structures, and oxidation states of the catalysts were then investigated by XPS (Figure 3). As can be seen from the Ni  $2p_{3/2}$  spectra presented in Figure 3a, in the case of the  $\text{Ni}_{100}$  catalyst, peaks corresponding to Ni metal and  $\text{Ni}(\text{OH})_2$  were observed at 852.1 and 855.6 eV, respectively, wherein the latter arose due to the fact that electrodeposition was performed in a water-based electrolyte. For the  $\text{Ni}_{94.6}\text{Mo}_{5.4}$  catalyst, peaks corresponding to Ni metal (852.15 eV), NiO (853.25 eV), and  $\text{Ni}(\text{OH})_2$  (855.65 eV) were observed, with the intensity of the Ni metal peak being significantly enhanced compared to that of  $\text{Ni}_{100}$ . This was attributed to the alloying of Ni with Mo, which has a lower electronegativity than Ni (i.e., 1.88 vs. 1.47 on the Allen electronegativity scale [42]). Notably, this leads to an increased electron density on the Ni d orbital, which lowers the hydrogen adsorption strength on the Ni surface and leads to faster HER kinetics [33]. Upon the addition of small amounts of Mn (i.e.,  $\text{Ni}_{82.1}\text{Mo}_{11.6}\text{Mn}_{6.3}$ ), the intensities of both the NiO and  $\text{Ni}(\text{OH})_2$  peaks decreased, whereas the relative ratio of the metallic Ni peak slightly increased compared to that observed for  $\text{Ni}_{94.6}\text{Mo}_{5.4}$ . This is likely due to the higher bulk Mo at% of 11.6 and the inclusion of Mn, which has a lower electronegativity (1.75 [42]) than Ni.

Similarly, the dominance of  $\text{MoO}_2$  peaks (228.9–232.05 and 229.05–232.2 eV) and  $\text{MoO}_3$  peaks (232.1–235.25 and 232.35–235.5 eV) in Mo  $3d_{5/2}$  spectrum of the  $\text{Ni}_{94.6}\text{Mo}_{5.4}$  catalyst (upper panel, Figure 3b), which was attributed to the electron transfer from Mo to Ni, has been relieved for the  $\text{Ni}_{82.1}\text{Mo}_{11.6}\text{Mn}_{6.3}$  composition (lower panel, Figure 3b). In addition, the relative portion of metallic Mo (227.45–230.6 and 227.45–230.9 eV) increased slightly from 36.3% to 47.1% at this composition. However, the incorporation of Mn and electron transfer from the Mn species to Ni are evident by the observation of strong  $\text{Mn}^{3+}$  (640.6 eV) and  $\text{Mn}^{4+}$  (642.3 eV) peaks in the Mn  $2p_{3/2}$  spectrum of  $\text{Ni}_{82.1}\text{Mo}_{11.6}\text{Mn}_{6.3}$  (Figure 3c). Furthermore, Figure 3d shows the O 1s spectra of the  $\text{Ni}_{100}$ ,  $\text{Ni}_{94.6}\text{Mo}_{5.4}$ , and  $\text{Ni}_{82.1}\text{Mo}_{11.6}\text{Mn}_{6.3}$  catalysts, which can be divided into M–O, M–OH, oxygen vacancy, and  $\text{H}_2\text{O}$  peaks. The proportion of M–O bonds appeared to be decreased in the order of  $\text{Ni}_{100} > \text{Ni}_{94.6}\text{Mo}_{5.4} > \text{Ni}_{82.1}\text{Mo}_{11.6}\text{Mn}_{6.3}$ , whereas the proportion of oxygen vacancies increased from 2.4 to 15.7% and 23.4%, respectively. Notably, an increase in the number of oxygen vacancies can enhance the catalyst activity by increasing the number of defect sites on the surface [43]. Based on the XPS analysis, it was therefore expected that the three different catalysts would exhibit different catalytic activities for the HER, as discussed in the following sections.

**3.2. Electrochemical Characterization of the Catalysts: HER Performance.** The HER activities of the prepared catalysts were evaluated, and their related electrochemical characterizations were performed, as outlined in Figure 4. More specifically, the HER performances of the  $\text{Ni}_{100}$ ,  $\text{Ni}_{94.6}\text{Mo}_{5.4}$ , and  $\text{Ni}_{82.1}\text{Mo}_{11.6}\text{Mn}_{6.3}$  catalysts were evaluated by CV using a three-electrode system at a scan rate of  $1 \text{ mV s}^{-1}$  in an acidic solution (0.5 M  $\text{H}_2\text{SO}_4$ ). Based on the iR-corrected HER polarization curves presented in Figure 4a, the slight reduction currents observed at approximately  $0 \text{ V}_{\text{RHE}}$  for the  $\text{Ni}_{94.6}\text{Mo}_{5.4}$  and  $\text{Ni}_{82.1}\text{Mo}_{11.6}\text{Mn}_{6.3}$  catalysts were potentially caused by the reduction of surface  $\text{MoO}_x$  species, which were generated during the electrodeposition process [25, 44]. The overpotential of  $\text{Ni}_{100}$  reached 153 mV at  $-10 \text{ mA cm}^{-2}$ , indicating that this species exhibited a low catalytic activity. In contrast,  $\text{Ni}_{94.6}\text{Mo}_{5.4}$  demonstrated low overpotentials of 21 and 49 mV at  $-10$  and  $-50 \text{ mA cm}^{-2}$ , respectively, while  $\text{Ni}_{82.1}\text{Mo}_{11.6}\text{Mn}_{6.3}$  exhibited dramatically reduced overpotentials of 16 and 28 mV at  $-10$  and  $-50 \text{ mA cm}^{-2}$ . Notably, these values are close to or superior to those of recently reported Pt-based HER catalysts [45–47]. To ensure a more accurate comparison with Pt catalyst, we evaluated the HER performance of Pt prepared by electrodeposition, and the results are presented in Figure S2. As clearly shown in the figure, the overpotential at  $-10 \text{ mA cm}^{-2}$  is 11 mV for the Pt catalyst, demonstrating approximately 5 mV better performance. However, this performance difference is reversed at around  $-20 \text{ mA cm}^{-2}$ , where the  $\text{Ni}_{82.1}\text{Mo}_{11.6}\text{Mn}_{6.3}$  catalyst exhibits superior performance in the high-current region. The HER activities of the other catalysts fabricated using a wider range of precursor concentrations are presented in Table S1, indicating that the  $\text{Ni}_{82.1}\text{Mo}_{11.6}\text{Mn}_{6.3}$  catalyst exhibited the best performance of all catalysts evaluated herein. Subsequently, Tafel plots were

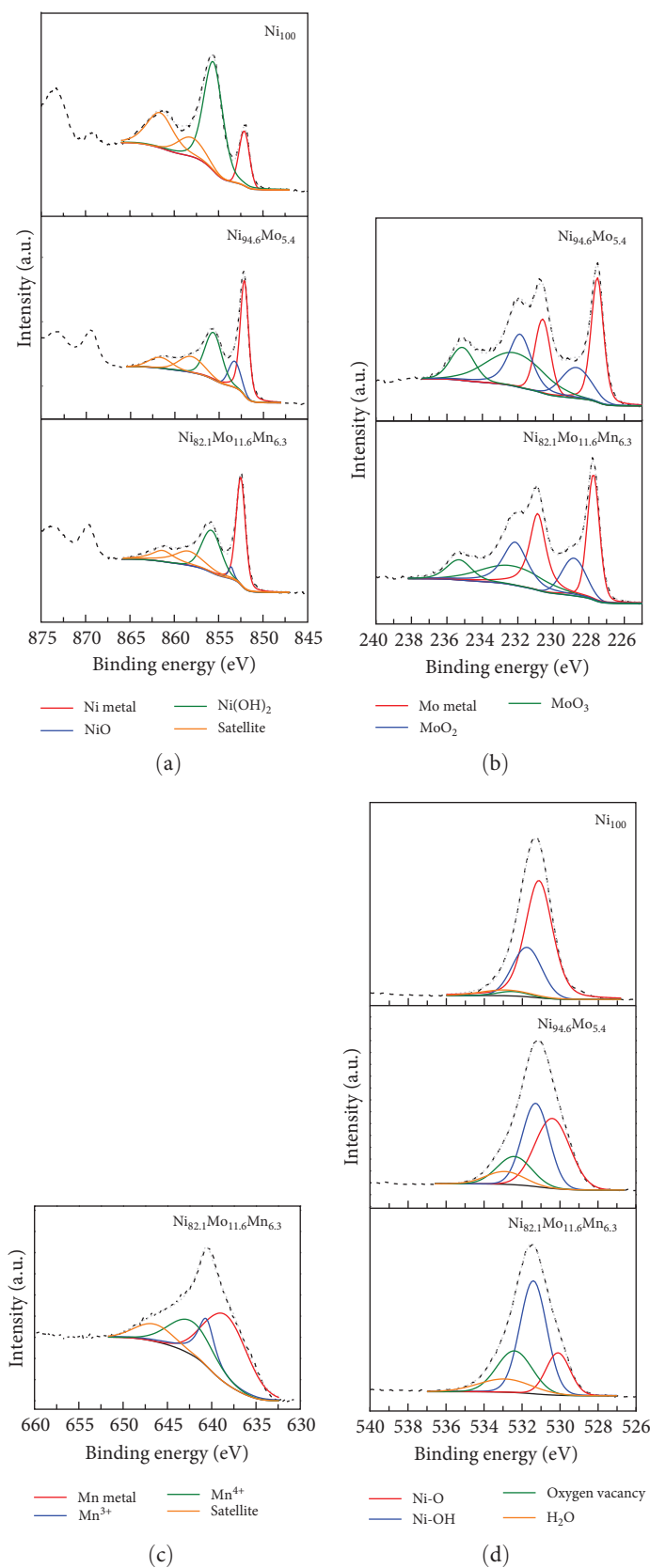


FIGURE 3: XPS spectra of the (a) Ni  $2p_{3/2}$ , (b) Mo  $3d_{5/2}$ , (c) Mn  $2p_{3/2}$ , and (d) O  $1s$  components of the  $Ni_{100}$ ,  $Ni_{94.6}Mo_{5.4}$ , and  $Ni_{82.1}Mo_{11.6}Mn_{6.3}$  species. The raw intensities are represented using dotted gray lines, while the obtained fittings are represented using dashed black lines.

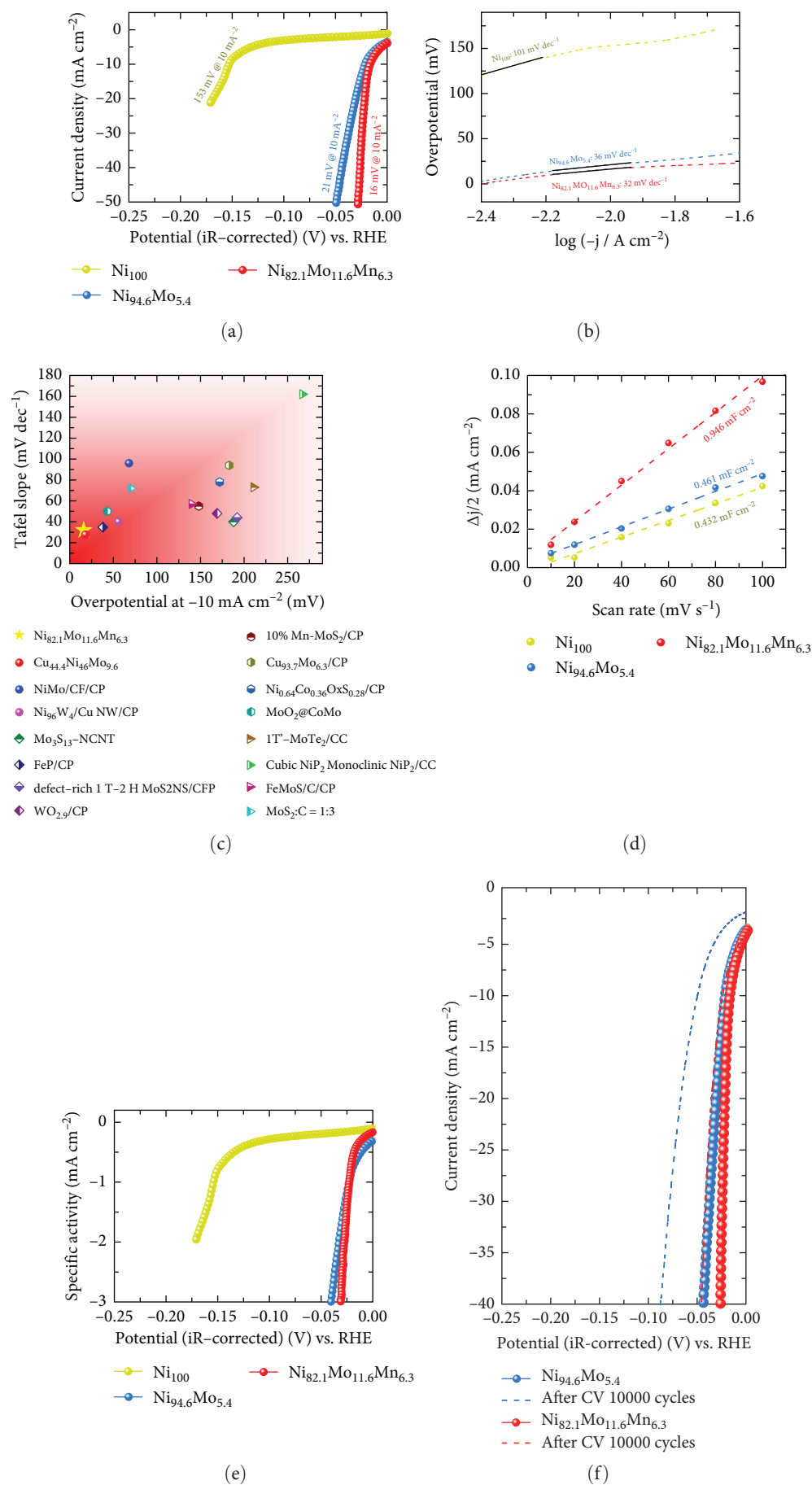


FIGURE 4: Continued.

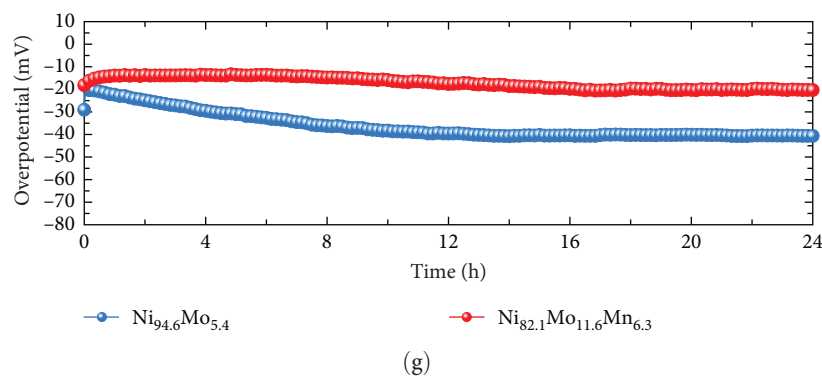


FIGURE 4: (a) HER polarization curves measured at a scan rate of  $1 \text{ mV s}^{-1}$  with iR-compensation. (b) HER Tafel plots derived from the curves presented in panel (a). (c) Comparison with reported nonprecious catalysts. (d) Measurement of the electrochemical double-layer capacitance ( $C_{dl}$ ) in a 1 M NaOH solution. (e) Specific activity. (f) HER polarization results for the 1st and 10,000th curves obtained for the  $\text{Ni}_{94.6}\text{Mo}_{5.4}$  and  $\text{Ni}_{82.1}\text{Mo}_{11.6}\text{Mn}_{6.3}$  species. (g) Chronopotentiometry results obtained over 24 h at  $-10 \text{ mA cm}^{-2}$  for the  $\text{Ni}_{94.6}\text{Mo}_{5.4}$  and  $\text{Ni}_{82.1}\text{Mo}_{11.6}\text{Mn}_{6.3}$  species.

obtained for the  $\text{Ni}_{100}$ ,  $\text{Ni}_{94.6}\text{Mo}_{5.4}$ , and  $\text{Ni}_{82.1}\text{Mo}_{11.6}\text{Mn}_{6.3}$  catalysts based on the HER polarization curves presented in Figure 4a. As can be seen from the corresponding results (Figure 4b),  $\text{Ni}_{100}$  possesses a Tafel slope of  $101 \text{ mV dec}^{-1}$ , implying that the Volmer (discharge) reaction is the rate-determining step. However,  $\text{Ni}_{94.6}\text{Mo}_{5.4}$  and  $\text{Ni}_{82.1}\text{Mo}_{11.6}\text{Mn}_{6.3}$  exhibit Tafel slopes of 36 and  $32 \text{ mV dec}^{-1}$ , respectively, suggesting that their HER processes follow the Volmer–Heyrovsky mechanism, although  $\text{Ni}_{82.1}\text{Mo}_{11.6}\text{Mn}_{6.3}$  tended toward the Volmer–Tafel mechanism. Figure 4c shows a comparison between  $\text{Ni}_{82.1}\text{Mo}_{11.6}\text{Mn}_{6.3}$  and other reported nonprecious metal catalysts at the half-cell level, while a more detailed comparison with previously reported nonprecious metal HER catalysts is presented in Table S2. As can be seen from the figure,  $\text{Ni}_{82.1}\text{Mo}_{11.6}\text{Mn}_{6.3}$  demonstrates an overwhelmingly small overpotential and fast reaction kinetics compared to previously reported nonprecious-metal acidic HER catalysts. Furthermore, the surface areas of the electrochemical reactions were compared by measuring the electrochemical charge double-layer capacitance ( $C_{dl}$ ), obtained from the differences between the anodic and cathodic currents during LSV at various scan rates within the nonfaradaic region in a 1 M NaOH solution (Figure S3). As shown in Figure 4d, the  $C_{dl}$  of  $\text{Ni}_{82.1}\text{Mo}_{11.6}\text{Mn}_{6.3}$  was  $0.946 \text{ mF cm}^{-2}$ , which represents the largest electrochemically active surface of the three catalysts (i.e.,  $\text{Ni}_{100} = 0.432 \text{ mF cm}^{-2}$ ,  $\text{Ni}_{94.6}\text{Mo}_{5.4} = 0.461 \text{ mF cm}^{-2}$ ). The roughness factor (RF) was further calculated by dividing the  $C_{dl}$  by the average reported capacitance value for Ni-containing metallic electrodes measured in a 1 M NaOH solution (i.e.,  $C_s = 0.04 \text{ mF cm}^{-2}$ ) [48]. The calculated RF values for the  $\text{Ni}_{100}$ ,  $\text{Ni}_{94.6}\text{Mo}_{5.4}$ , and  $\text{Ni}_{82.1}\text{Mo}_{11.6}\text{Mn}_{6.3}$  catalysts were determined to be 10.8, 11.5, and 23.6, respectively. These values are consistent with the activity trend of the HER polarization curves shown in Figure 4a, indicating that the enlarged electrochemical surface area contributes to the superior HER activity of  $\text{Ni}_{82.1}\text{Mo}_{11.6}\text{Mn}_{6.3}$ . The HER activities normalized to the RF values (specific activities) were also compared to identify the intrinsic activities of the catalysts. As shown in Figure 4e,  $\text{Ni}_{82.1}\text{Mo}_{11.6}\text{Mn}_{6.3}$  demonstrated the highest performance in terms of both its geometric and specific activities, especially in the high-current range.

**3.3. Evaluation of the Catalyst Durability.** The durability of a nonprecious-metal catalyst in an acidic environment is crucial due to its vulnerability to corrosive environments. Thus, to evaluate the practical feasibility of the developed catalysts for application in commercial PEMWE systems, an ADT and a constant-current durability test were performed, as presented in Figure 4f and g, respectively. The ADT test was conducted by carrying out 10,000 CV cycles over a potential range of  $-0.2$  to  $0.05 V_{RHE}$ . As shown in Figure 4f, the overpotential of the as-prepared  $\text{Ni}_{94.6}\text{Mo}_{5.4}$  increased from 21 to 49 mV after 10,000 CV cycles at  $-10 \text{ mA cm}^{-2}$ , indicating a stark deterioration of the catalyst activity. The deterioration of the catalyst is clearly evident, as shown in Figure S4a, where it progressively occurs after 3,000, 5,000, and 10,000 cycles. However, only an 8 mV increase in the overpotential was observed at  $-10 \text{ mA cm}^{-2}$  in the case of the catalyst  $\text{Ni}_{82.1}\text{Mo}_{11.6}\text{Mn}_{6.3}$  after 10,000 CV cycles (i.e., from 16 to 24 mV), thereby confirming its remarkable electrochemical durability. Notably, in contrast to  $\text{Ni}_{94.6}\text{Mo}_{5.4}$  degradation of  $\text{Ni}_{82.1}\text{Mo}_{11.6}\text{Mn}_{6.3}$  ceases after 3,000 cycles with performance remaining relatively stable up to 10,000 cycles (Figure S4b). To further evaluate the potential for durability enhancement, the  $\text{Ni}_{82.1}\text{Mo}_{11.6}\text{Mn}_{6.3}$  catalyst underwent heat treatment at  $200^\circ\text{C}$  for 2 h in a 4%  $\text{H}_2/\text{Ar}$  atmosphere, followed by the same ADT evaluation. The results, presented in Figure S5, reveal a slight performance degradation, as evidenced by an increase in overpotential at  $-10 \text{ mA cm}^{-2}$  from 16 mV to 39 mV. In terms of durability, a 9 mV increase in overpotential was observed after 10,000 cycles. These findings suggest that heat treatment has a minimal and ineffective impact on both catalyst performance and durability. Secondly, the constant-current durability was assessed at a current density of  $-10 \text{ mA cm}^{-2}$ . As shown in Figure 4g,  $\text{Ni}_{94.6}\text{Mo}_{5.4}$  demonstrated a rapid increase in overpotential during the initial 8 h, reaching 40 mV at the end of the test. In contrast,  $\text{Ni}_{82.1}\text{Mo}_{11.6}\text{Mn}_{6.3}$  showed no sharp overpotential increase during the initial stages of the test, instead demonstrating a slight initial decrease followed by a gentle increase, leading to a final overpotential of 20 mV. The corresponding degradation rates were determined to be  $0.75 \text{ mV h}^{-1}$  for  $\text{Ni}_{94.6}\text{Mo}_{5.4}$  and  $0.125 \text{ mV h}^{-1}$  for  $\text{Ni}_{82.1}\text{Mo}_{11.6}\text{Mn}_{6.3}$ , indicating the excellent

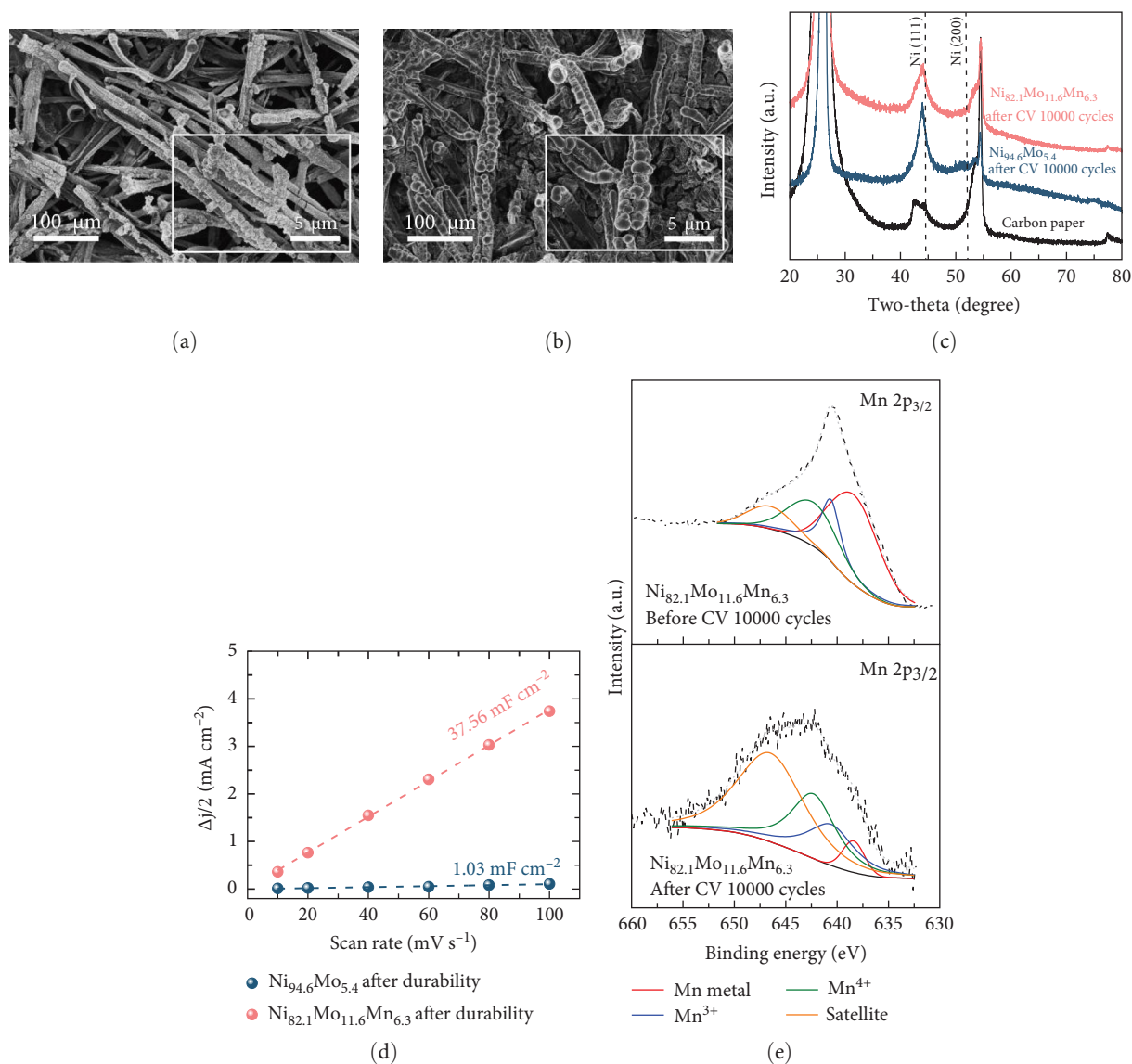


FIGURE 5: Characterization results after 10,000 CV cycles. FE-SEM images of the (a)  $\text{Ni}_{94.6}\text{Mo}_{5.4}$ , (b)  $\text{Ni}_{82.1}\text{Mo}_{11.6}\text{Mn}_{6.3}$  species, (c) XRD patterns, (d)  $C_{dl}$  measurements, and (e) XPS Mn 2p<sub>3/2</sub> spectra.

durability of  $\text{Ni}_{82.1}\text{Mo}_{11.6}\text{Mn}_{6.3}$  in an acidic electrolyte. The durability of the  $\text{Ni}_{82.1}\text{Mo}_{11.6}\text{Mn}_{6.3}$  catalyst was further compared with those of previously reported nonprecious metal HER catalysts (Table S2).

Following the durability test, and particularly after the harsher ADT, the physicochemical changes in the  $\text{Ni}_{82.1}\text{Mo}_{11.6}\text{Mn}_{6.3}$  catalyst were investigated. Compared with the SEM images presented in Figure 1b, it can be seen that the morphology of  $\text{Ni}_{94.6}\text{Mo}_{5.4}$  after the ADT (Figure 5a) was significantly changed, with substantial parts of the deposits being peeled from the carbon fiber surface, indicating dissolution of the deposits. Similarly, the  $\text{Ni}_{82.1}\text{Mo}_{11.6}\text{Mn}_{6.3}$  catalyst also demonstrated a slight degree of dissolution after the ADT (Figure 5b), generating spherical particles rather than a smooth surface (see Figure 1c), while maintaining its overall coverage on the carbon fiber. Catalyst dissolution was confirmed by XRD analysis, as shown in Figure 5c. More

specifically, for both the  $\text{Ni}_{94.6}\text{Mo}_{5.4}$  and  $\text{Ni}_{82.1}\text{Mo}_{11.6}\text{Mn}_{6.3}$  catalysts, the intensities of the main Ni (111) and Ni (200) peaks decreased, indicating dissolution and flaking of the bulk catalyst layer during ADT. As shown in Figure 5d, catalyst dissolution significantly affected the electrochemical surface area, with a more pronounced effect being observed for the  $\text{Ni}_{82.1}\text{Mo}_{11.6}\text{Mn}_{6.3}$  catalyst. In this case, the  $C_{dl}$  value of the  $\text{Ni}_{94.6}\text{Mo}_{5.4}$  catalyst increased from 0.461 to 1.03  $\text{mF cm}^{-2}$  following the ADT, while that of the  $\text{Ni}_{82.1}\text{Mo}_{11.6}\text{Mn}_{6.3}$  catalyst increased significantly from 0.946 to 37.56  $\text{mF cm}^{-2}$ , indicating approximately 40-fold increase in the surface area. This compensates for active site dissolution to maintain excellent catalytic performance.

To identify changes in the surface elemental composition during the ADT, XPS analysis was conducted, and the results are outlined in Table S3. The surface composition of  $\text{Ni}_{94.6}\text{Mo}_{5.4}$  was defined as  $\text{Ni}_{76.0}\text{Mo}_{24.0}$  prior to the ADT, and this changed to

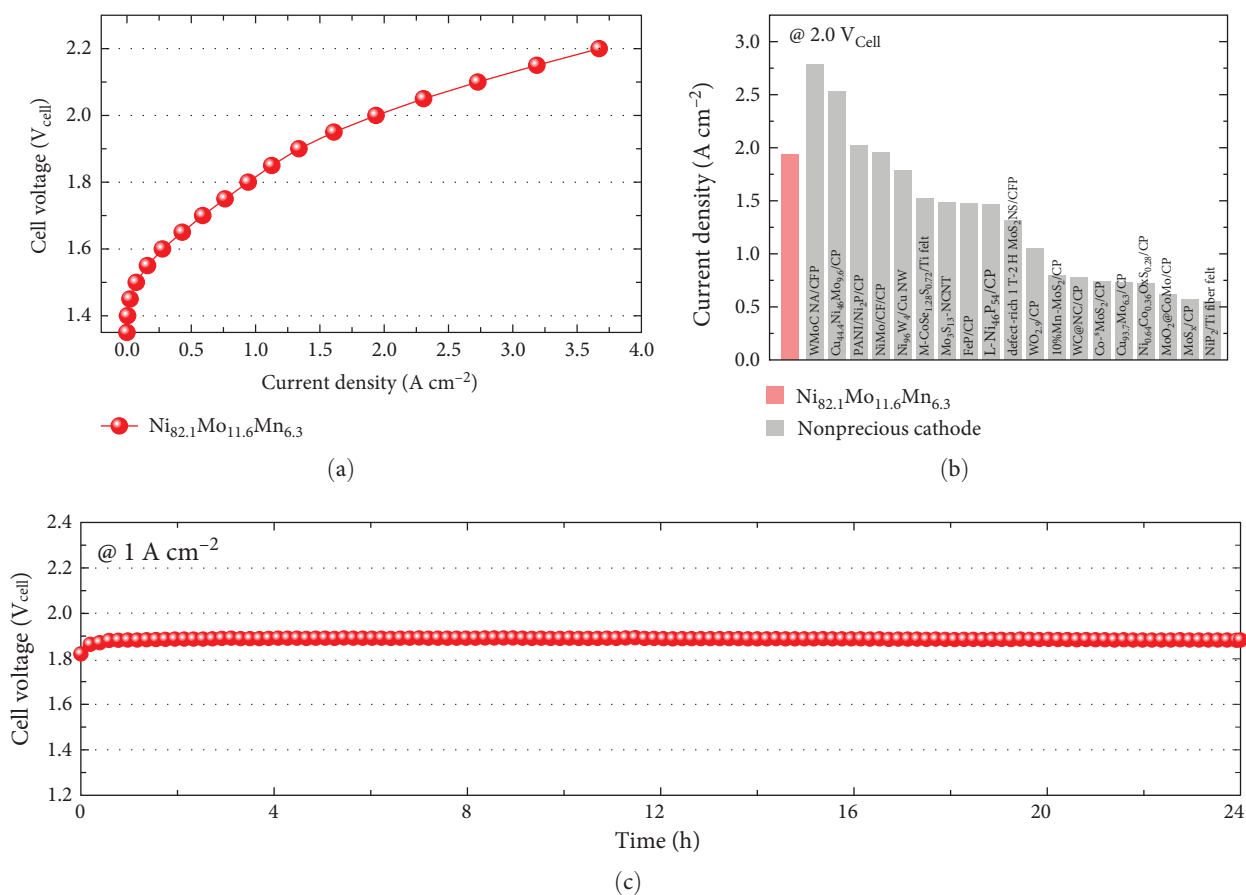


FIGURE 6: (a) Single-cell polarization curves recorded using the Ni<sub>82.1</sub>Mo<sub>11.6</sub>Mn<sub>6.3</sub> cathode. (b) Performance comparison with reported nonprecious cathodes in terms of cell current density at 2.0 V<sub>cell</sub>. (c) Long-term stability measurements performed at a current density of 1 A cm<sup>-2</sup> for 24 h.

Ni<sub>79.6</sub>Mo<sub>20.4</sub> after the ADT. The difference between the bulk composition (Ni<sub>94.6</sub>Mo<sub>5.4</sub>) and the surface composition (Ni<sub>76.0</sub>Mo<sub>24.0</sub>) before the ADT implied that the catalyst surface was Mo-rich [49]. This surface-enriched Mo underwent dissolution during the ADT, reducing the Mo surface content from 24.0% to 20.4%, leading to an increase in the Ni surface content from 76.0% to 79.6%. During the potential range used for the ADT, Mo can exist as Mo<sup>3+</sup>, MoO<sub>2</sub>, and MoO<sub>4</sub><sup>2-</sup> ions depending on the pH [50]. Considering that the local pH near the cathode can exceed 7 even under acidic HER conditions [51], all three oxidation states are possible in this potential range. The larger Ni content and smaller Mo content after ADT may therefore alter the electronic structure of Ni and have a detrimental effect on the HER. However, a recent study [52] predicted that some nonstoichiometric Mn oxide phases, such as spinel Mn<sub>3</sub>O<sub>4</sub> and cubic Mn<sub>2</sub>O<sub>3</sub>, are stable in large regions of the potential-pH diagram. Indeed, this was confirmed by XPS analysis of the Ni<sub>82.1</sub>Mo<sub>11.6</sub>Mn<sub>6.3</sub> catalyst (Table S3), wherein it was found that the as-prepared catalyst had a surface composition of Ni<sub>70.7</sub>Mo<sub>27.8</sub>Mn<sub>1.5</sub>, which changed to Ni<sub>82.3</sub>Mo<sub>13.1</sub>Mn<sub>4.6</sub> after the ADT. Thus, during the ADT, significant dissolution of both Ni and Mo was observed, as in the case of the Ni<sub>94.6</sub>Mo<sub>5.4</sub> catalyst, while the surface content of Mn increased from 1.5% to 4.6%. This enriched Mn content after ADT compensated for the loss of Mo and provided electrons to Ni to maintain an

optimal level of hydrogen adsorption on the Ni species. This was verified from XPS analysis of the Mn species before and after the ADT (Figure 5e). More specifically, after the ADT, the intensities of the peaks corresponding to metallic Mn and Mn<sup>3+</sup> decreased significantly (i.e., from 46.93% to 8.55% and from 19.02% to 10.06%, respectively). However, the proportion of Mn<sup>4+</sup> increased (i.e., from 10.51% to 33.16%), indicating a higher oxidation state than those of the stable nonstoichiometric Mn<sub>3</sub>O<sub>4</sub> and Mn<sub>2</sub>O<sub>3</sub> species. This implies that electron transfer occurred from Mn (in the Mn oxide) to Ni to compensate for the loss of Mo. Thus, in combination with the enlarged surface area, stable Mn oxide formation on the surface during ADT was responsible for the enhanced durability of the Ni<sub>82.1</sub>Mo<sub>11.6</sub>Mn<sub>6.3</sub> catalyst.

**3.4. Evaluation of the Catalyst PEMWE Performance and Durability.** Considering the excellent activity and durability demonstrated in the half-cell test of the Ni<sub>82.1</sub>Mo<sub>11.6</sub>Mn<sub>6.3</sub> catalyst, this material was employed as the cathode in a PEMWE single cell. The MEA was fabricated by sandwiching the sprayed IrO<sub>2</sub>/CP anode and the Ni<sub>82.1</sub>Mo<sub>11.6</sub>Mn<sub>6.3</sub>/CP cathode on opposite sides of a Nafion 212 proton-exchange membrane. As shown in Figure 6a, the Ni<sub>82.1</sub>Mo<sub>11.6</sub>Mn<sub>6.3</sub> cathode-embedded PEMWE exhibited a performance of 1.936 A cm<sup>-2</sup> at 2.0 V<sub>cell</sub>. This performance is relatively high

compared to those of previously reported nonprecious metal HER catalysts applied to the PEMWE, as summarized in Figure 6b and Table S4. To confirm the catalyst durability obtained from the half-cell experiments, a constant-current PEMWE operation was performed at  $1 \text{ A cm}^{-2}$ . As presented in Figure 6c, following the initial increase after 1 h of operation, a stable cell voltage of approximately  $1.883 \text{ V}_{\text{cell}}$  was maintained, thereby confirming excellent durability. To assess catalyst leaching from the electrode during the durability test, ICP-MS analysis was performed, and the results are summarized in Table S5. The leached metal content was quantified by collecting the effluent discharged from the single cell over 24 h and analyzing it via ICP-MS. As shown in Table S5, the total metal leaching over 24 h was approximately  $1.6 \text{ mg cm}^{-2}$ , corresponding to a normalized rate of approximately  $0.068 \text{ mg cm}^{-2} \text{ h}^{-1}$ . These results indicate that metal dissolution during operation is minimal, and even this minimal dissolution can be further reduced, as supported by recent research findings, such as the acid treatment of carbon paper [53]. Overall, these results confirm the feasibility of  $\text{Ni}_{82.1}\text{Mo}_{11.6}\text{Mn}_{6.3}$  for use as a nonprecious metal cathode material for commercialization.

#### 4. Conclusions

A wide range of NiMoMn ternary alloy catalysts consisting of different component ratios were investigated for application as nonprecious metal HER catalysts for PEMWE. For this purpose, a one-step electrodeposition approach was employed to enable rapid screening by regulating the precursor content of the electrolyte. The half-cell performance of the optimal  $\text{Ni}_{82.1}\text{Mo}_{11.6}\text{Mn}_{6.3}$  catalyst was evaluated, giving an overpotential of 16 mV at  $-10 \text{ mA cm}^{-2}$ , and a Tafel slope of  $32 \text{ mV dec}^{-1}$  in a  $0.5 \text{ M H}_2\text{SO}_4$  solution. It was found that the incorporation of Mn modulated the electronic structure of the original NiMo catalyst, in addition to increasing the electrochemical surface area and number of oxygen vacancies, which simultaneously contributed to an excellent HER activity. Notably, the  $\text{Ni}_{82.1}\text{Mo}_{11.6}\text{Mn}_{6.3}$  catalyst demonstrated excellent durability in an ADT over 10,000 CV cycles, with an overpotential increase of only 8 mV being recorded while maintaining a good overall coverage on the carbon fiber substrate. The enhanced durability of the  $\text{Ni}_{82.1}\text{Mo}_{11.6}\text{Mn}_{6.3}$  catalyst was attributed to two key factors, namely its enlarged surface area and the formation of stable Mn oxides, which can compensate for the loss of Mo on the surface during the ADT. Upon the application of  $\text{Ni}_{82.1}\text{Mo}_{11.6}\text{Mn}_{6.3}$  as a cathode material in PEMWE, a performance of  $1.936 \text{ A cm}^{-2}$  was achieved at  $2.0 \text{ V}_{\text{cell}}$ , along with a decay rate of  $2.2 \text{ mV h}^{-1}$  during a 24 h durability test at  $1 \text{ A cm}^{-2}$ . The superior performance and stability of  $\text{Ni}_{82.1}\text{Mo}_{11.6}\text{Mn}_{6.3}$  suggest its potential for application as a nonprecious metal HER electrode to reduce the cost of hydrogen production by PEMWE.

#### Data Availability Statement

The data supporting the findings of this study are available from the corresponding author upon reasonable request.

#### Conflicts of Interest

The authors declare no conflicts of interest.

#### Author Contributions

Chan Hee Lee: conceptualization, formal analysis, investigation, methodology, and writing—original draft. Kyeong-Rim Yeo: formal analysis and investigation. Soo-Kil Kim: conceptualization, funding acquisition, methodology, project administration, supervision, and writing—review & editing.

#### Funding

This work was supported by the National Research Foundation of Korea (NRF) grant funded by the Korean Government (MSIT) (RS-2024-00409901, RS-2024-00413272, and RS-2024-00340074).

#### Supporting Information

Additional supporting information can be found online in the Supporting Information section. (*Supporting Information*) Supporting data related to this article can be found online in the Supporting Information section.

#### References

- [1] T. M. Gür, "Review of Electrical Energy Storage Technologies, Materials and Systems: Challenges and Prospects for Large-Scale Grid Storage," *Energy & Environmental Science* 11, no. 10 (2018): 2696–2767.
- [2] A. Odenweller, F. Ueckerdt, G. F. Nemet, M. Jensterle, and G. Luderer, "Probabilistic Feasibility Space of Scaling up Green Hydrogen Supply," *Nature Energy* 7, no. 9 (2022): 854–865.
- [3] T. Lim and S.-K. Kim, "Non-Precious Hydrogen Evolution Reaction Catalysts: Stepping Forward to Practical Polymer Electrolyte Membrane-Based Zero-Gap Water Electrolyzers," *Chemical Engineering Journal* 433 (2022): 133681.
- [4] M. Zeng and Y. Li, "Recent Advances in Heterogeneous Electrocatalysts for the Hydrogen Evolution Reaction," *Journal of Materials Chemistry A* 3, no. 29 (2015): 14942–14962.
- [5] W. Zhai, Y. Ma, D. Chen, J. C. Ho, Z. Dai, and Y. Qu, "Recent Progress on the Long-Term Stability of Hydrogen Evolution Reaction Electrocatalysts," *InfoMat* 4, no. 9 (2022): 2022–e12357.
- [6] X.-L. Zhang, P.-C. Yu, X.-Z. Su, et al., "Efficient Acidic Hydrogen Evolution in Proton Exchange Membrane Electrolyzers over a Sulfur-Doped Marcasite-Type Electrocatalyst," *Science Advances* 9, no. 27 (2023): 2023–eadh2885.
- [7] X. Xiong, J. Tang, Y. Ji, et al., "High-Efficiency Iridium-Yttrium Alloy Catalyst for Acidic Water Electrolysis," *Advanced Energy Materials* 14, no. 20 (2024): 2304479.
- [8] J. Wang, F. Xu, H. Jin, Y. Chen, and Y. Wang, "Non-Noble Metal-Based Carbon Composites in Hydrogen Evolution Reaction: Fundamentals to Applications," *Advanced Materials* 29, no. 14 (2017): 1605838.
- [9] P. Chen, J. Ye, H. Wang, L. Ouyang, and M. Zhu, "Recent Progress of Transition Metal Carbides/Nitrides for Electrocatalytic Water Splitting," *Journal of Alloys and Compounds* 883 (2021): 160833.
- [10] Y. Shi and B. Zhang, "Recent Advances in Transition Metal Phosphide Nanomaterials: Synthesis and Applications in

- Hydrogen Evolution Reaction,” *Chemical Society Reviews* 45, no. 6 (2016): 1529–1541.
- [11] A. B. Laursen, R. B. Wexler, M. J. Whitaker, et al., “Climbing the Volcano of Electrocatalytic Activity while Avoiding Catalyst Corrosion: Ni<sub>3</sub>P, a Hydrogen Evolution Electrocatalyst Stable in Both Acid and Alkali,” *ACS Catalysis* 8, no. 5 (2018): 4408–4419.
- [12] J. F. Callejas, C. G. Read, E. J. Popczun, J. M. McEnaney, and R. E. Schaak, “Nanostructured Co<sub>2</sub>P Electrocatalyst for the Hydrogen Evolution Reaction and Direct Comparison with Morphologically Equivalent CoP,” *Chemistry of Materials* 27, no. 10 (2015): 3769–3774.
- [13] W. Xiao, L. Zhang, D. Bukhvalov, et al., “Hierarchical Ultrathin Carbon Encapsulating Transition Metal Doped MoP Electrocatalysts for Efficient and pH-Universal Hydrogen Evolution Reaction,” *Nano Energy* 70 (2020): 104445.
- [14] D. Y. Chung, S. W. Jun, G. Yoon, et al., “Large-Scale Synthesis of Carbon-Shell-Coated FeP Nanoparticles for Robust Hydrogen Evolution Reaction Electrocatalyst,” *Journal of the American Chemical Society* 139, no. 19 (2017): 6669–6674.
- [15] X. Zhao, Z. Zhang, X. Cao, et al., “Elucidating the Sources of Activity and Stability of FeP Electrocatalyst for Hydrogen Evolution Reactions in Acidic and Alkaline Media,” *Applied Catalysis B: Environmental* 260 (2020), 118156.
- [16] J. Kibsgaard, Z. Chen, B. N. Reinecke, and T. F. Jaramillo, “Engineering the Surface Structure of MoS<sub>2</sub> to Preferentially Expose Active Edge Sites for Electrocatalysis,” *Nature Materials* 11, no. 11 (2012): 963–969.
- [17] T. F. Jaramillo, K. P. Jørgensen, J. Bonde, J. H. Nielsen, S. Horch, and I. Chorkendorff, “Identification of Active Edge Sites for Electrochemical H<sub>2</sub> Evolution from MoS<sub>2</sub> Nanocatalysts,” *Science* 317, no. 5834 (2007): 100–102.
- [18] J. Xie, H. Qu, J. Xin, et al., “Defect-Rich MoS<sub>2</sub> Nanowall Catalyst for Efficient Hydrogen Evolution Reaction,” *Nano Research* 10 (2017): 1178–1188.
- [19] T. V. Nguyen, M. Tekalgne, C. V. Tran, et al., “Synthesis of MoS<sub>2</sub>/WS<sub>2</sub> Nanoflower Heterostructures for Hydrogen Evolution Reaction,” *International Journal of Energy Research* 2024, no. 1 (2024): 3192642.
- [20] P. Xiao, X. Ge, H. Wang, Z. Liu, A. Fisher, and X. Wang, “Novel Molybdenum Carbide-Tungsten Carbide Composite Nanowires and Their Electrochemical Activation for Efficient and Stable Hydrogen Evolution,” *Advanced Functional Materials* 25, no. 10 (2015): 1520–1526.
- [21] E. Navarro-Flores, Z. Chong, and S. Omanovic, “Characterization of Ni, NiMo, NiW and NiFe Electroactive Coatings as Electrocatalysts for Hydrogen Evolution in an Acidic Medium,” *Journal of Molecular Catalysis A: Chemical* 226, no. 2 (2005): 179–197.
- [22] H. Nady and M. Negem, “Ni-Cu Nano-Crystalline Alloys for Efficient Electrochemical Hydrogen Production in Acid Water,” *RSC Advances* 6, no. 56 (2016): 51111–51119.
- [23] J. Deng, P. Ren, D. Deng, and X. Bao, “Enhanced Electron Penetration through an Ultrathin Graphene Layer for Highly Efficient Catalysis of the Hydrogen Evolution Reaction,” *Angewandte Chemie International Edition* 54, no. 7 (2015): 2100–2104.
- [24] H. Kim, H. Park, S. Oh, and S. K. Kim, “Facile Electrochemical Preparation of Nonprecious Co-Cu Alloy Catalysts for Hydrogen Production in Proton Exchange Membrane Water Electrolysis,” *International Journal of Energy Research* 44, no. 4 (2019): 2833–2844.
- [25] H. Kim, E. Hwang, H. Park, et al., “Non-Precious Metal Electrocatalysts for Hydrogen Production in Proton Exchange Membrane Water Electrolyzer,” *Applied Catalysis B: Environmental* 206 (2017): 608–616.
- [26] H. Wang, Y. Yang, J. Liu, et al., “The Role of Manganese-Based Catalyst in Electrocatalytic Water Splitting,” *Recent Research and Progress, Materials Today Physics* (2023): 101169.
- [27] T. Liu, X. Ma, D. Liu, et al., “Mn Doping of CoP Nanosheets Array: An Efficient Electrocatalyst for Hydrogen Evolution Reaction with Enhanced Activity at All pH Values,” *ACS Catalysis* 7, no. 1 (2017): 98–102.
- [28] W. Guo, H. Kim, S. Hong, S. Y. Kim, and S. H. Ahn, “Constructing a NiMnS Electrode with a Mn-Rich Surface for Hydrogen Production in Anion Exchange Membrane Water Electrolyzers,” *Dalton Transactions* 52, no. 39 (2023): 14039–14046.
- [29] K. J. Choi, H. Kim, and S.-K. Kim, “Multicomponent Nonprecious Hydrogen Evolution Catalysts for High Performance and Durable Proton Exchange Membrane Water Electrolyzer,” *Journal of Power Sources* 506 (2021): 232000.
- [30] T. Wang, Y. Guo, Z. Zhou, X. Chang, J. Zheng, and X. Li, “Ni-Mo Nanocatalysts on N-Doped Graphite Nanotubes for Highly Efficient Electrochemical Hydrogen Evolution in Acid,” *ACS Nano* 10, no. 11 (2016): 10397–10403.
- [31] Y. Zhang, Y. Wang, S. Jia, et al., “A Hybrid of NiMo-Mo<sub>2</sub>C/C as Non-Noble Metal Electrocatalyst for Hydrogen Evolution Reaction in an Acidic Solution,” *Electrochimica Acta* 222 (2016): 747–754.
- [32] S. Martinez, M. Metikoš-Huković, and L. Valek, “Electrocatalytic Properties of Electrodeposited Ni-15Mo Cathodes for the HER in Acid Solutions: Synergistic Electronic Effect,” *Journal of Molecular Catalysis A: Chemical* 245, no. 1-2 (2006): 114–121.
- [33] J. R. McKone, B. F. Sadler, C. A. Werlang, N. S. Lewis, and H. B. Gray, “Ni-Mo Nanopowders for Efficient Electrochemical Hydrogen Evolution,” *ACS Catalysis* 3, no. 2 (2013): 166–169.
- [34] K.-R. Yeo, K.-S. Lee, H. Kim, J. Lee, and S.-K. Kim, “A Highly Active and Stable 3D Dandelion Spore-Structured Self-Supporting Ir-Based Electrocatalyst for Proton Exchange Membrane Water Electrolysis Fabricated Using Structural Reconstruction,” *Energy & Environmental Science* 15, no. 8 (2022): 3449–3461.
- [35] K.-R. Yeo, H. Kim, K.-S. Lee, et al., “Controlled Doping of Ultralow Amounts Ru on Ni Cathode for PEMWE: Experimental and Theoretical Elucidation of Enhanced Performance,” *Applied Catalysis B: Environmental and Energy* 346 (2024): 123738.
- [36] F. H. Assaf, M. M. Abou-Krishna, W. M. Daoush, and A. A. Eissa, “Fabrication of Zn-Ni-Mn Alloy by Electrodeposition and Its Characterization,” *Corrosion Reviews* 36, no. 6 (2018): 547–558.
- [37] H. Kazimierzak, A. Hara, A. Bigos, and P. Ozga, “Electrodeposition of Zn-Mn-Mo Layers from Citrate-Based Aqueous Electrolytes,” *Electrochimica Acta* 202 (2016): 110–121.
- [38] B. Abedini, N. P. Ahmadi, S. Yazdani, and L. Magagnin, “Electrodeposition and Corrosion Behavior of Zn–Ni–Mn Alloy Coatings Deposited from Alkaline Solution,” *Transactions of Nonferrous Metals Society of China* 30, no. 2 (2020): 548–558.
- [39] H. S. Park, K.-R. Yeo, W. S. Jung, and S.-K. Kim, “Electrodeposited Ternary CuNiMo Catalysts for Alkaline Hydrogen Oxidation,” *Electronic Materials Letters* 20, no. 3 (2024): 293–305.
- [40] H. T. Bang, K. R. Yeo, K. J. Choi, W. S. Jung, and S. K. Kim, “Ternary Ni-Mo-P Catalysts for Enhanced Activity and Durability

- in Proton Exchange Membrane Water Electrolysis,” *International Journal of Energy Research* 46, no. 9 (2022): 13023–13034.
- [41] H. Kim, H. Park, D. S. Tran, and S.-K. Kim, “Facile Fabrication of Amorphous NiMo Catalysts for Alkaline Hydrogen Oxidation Reaction,” *Journal of Industrial and Engineering Chemistry* 94 (2021): 309–316.
- [42] M. J. Winter, “Electronegativity(Allen),” 1993, (Accessed Nov 19 2024) [https://winter.group.shef.ac.uk/webelements/periodicity/eneg\\_allen/](https://winter.group.shef.ac.uk/webelements/periodicity/eneg_allen/).
- [43] B. Dasgupta, Y. Ren, L. M. Wong, et al., “Detrimental Effects of Oxygen Vacancies in Electrochromic Molybdenum Oxide,” *The Journal of Physical Chemistry C* 119, no. 19 (2015): 10592–10601.
- [44] G. H. Han, H. Kim, J. Kim, J. Kim, S. Y. Kim, and S. H. Ahn, “Micro-Nanoporous MoO<sub>2</sub>@CoMo Heterostructure Catalyst for Hydrogen Evolution Reaction,” *Applied Catalysis B: Environmental* 270 (2020): 118895.
- [45] K. Huang, R. Wang, H. Wu, et al., “Direct Immobilization of an Atomically Dispersed Pt Catalyst by Suppressing Heterogeneous Nucleation at – 40° C,” *Journal of Materials Chemistry A* 7, no. 45 (2019): 25779–25784.
- [46] J. Gao, X. Tang, P. Du, et al., “Synergistically Coupling Ultrasmall PtCu Nanoalloys with Highly Porous CoP Nanosheets as an Enhanced Electrocatalyst for Electrochemical Hydrogen Evolution,” *Sustainable Energy & Fuels* 4, no. 5 (2020): 2551–2558.
- [47] L. Lin, Z. Sun, M. Yuan, et al., “Significant Enhancement of the Performance of Hydrogen Evolution Reaction through Shape-Controlled Synthesis of Hierarchical Dendrite-Like Platinum,” *Journal of Materials Chemistry A* 6, no. 17 (2018): 8068–8077.
- [48] C. C. L. McCrory and S. Jung, “Benchmarking Heterogeneous Electrocatalysts for the Oxygen Evolution Reaction,” *Journal of the American Chemical Society*, 2013.
- [49] Y. Yu, J. Zhang, W. Xiao, J. Wang, and L. Wang, “First-Principles Study of Surface Segregation in Bimetallic Ni<sub>3</sub>M (M = Mo, Co, Fe) Alloys with Chemisorbed Atomic Oxygen,” *Physica Status Solidi (b)* 254, no. 6 (2017): 1600810.
- [50] D. Raj, F. Scaglione, G. Fiore, F. Celegato, and P. Rizzi, “Nanostructured Molybdenum Oxides from Aluminium-Based Intermetallic Compound: Synthesis and Application in Hydrogen Evolution Reaction,” *Nanomaterials* 11, no. 5 (2021).
- [51] K. Nagita, S. Nakanishi, and Y. Mukoyama, “Finite Element Analysis of Local pH Variations in Electrolysis with Porous Electrodes, Considering Water Self-Ionization,” *ACS Applied Materials & Interfaces* 16, no. 43 (2024): 59443–59451.
- [52] K. Wang, J. Han, A. Y. Gerard, J. R. Scully, and B.-C. Zhou, “Potential-pH Diagrams considering Complex Oxide Solution Phases for Understanding Aqueous Corrosion of Multi-Principal Element Alloys,” *NPJ Materials Degradation* 4, no. 1 (2020): 35.
- [53] J. Ma, J. H. Cho, C. Lee, et al., “Unraveling the Harmonious Coexistence of Ruthenium States on a Self-Standing Electrode for Enhanced Hydrogen Evolution Reaction,” *Energy & Environmental Materials* 7, no. 6 (2024): e12766.